nature physics

LETTERS

PUBLISHED ONLINE: 1 MAY 2011 | DOI: 10.1038/NPHYS1992

Twin-atom beams

Robert Bücker[1], Julian Grond[1,2,3†], Stephanie Manz[1], Tarik Berrada[1], Thomas Betz[1], Christian Koller[1], Ulrich Hohenester[2], Thorsten Schumm[1,3], Aurélien Perrin[1,3†] and Jörg Schmiedmayer[1*]

In recent years, substantial progress has been made in exploring and exploiting the analogy between classical light and matter waves for fundamental investigations and applications[1]. Extending this analogy to quantum matter-wave optics is promoted by the nonlinearities intrinsic to interacting particles and is a stepping stone towards non-classical states[2,3]. In light optics, twin-photon beams[4] are a key element for generating the non-local correlations and entanglement required for applications such as precision metrology and quantum communication[5]. Similar sources for massive particles have so far been limited by the multi-mode character of the processes involved or a predominant background signal[6–13]. Here we present highly efficient emission of twin-atom beams into a single transversal mode of a waveguide potential. The source is a one-dimensional degenerate Bose gas[14] in the first radially excited state. We directly measure a suppression of fluctuations in the atom number difference between the beams to 0.37(3) with respect to the classical expectation, equivalent to 0.11(2) after correcting for detection noise. Our results underline the potential of ultracold atomic gases as sources for quantum matter-wave optics and should enable the implementation of schemes previously unattainable with massive particles[5,15–19].

Binary collisions between atoms provide a natural means to generate dual number states of intrinsically correlated atoms[15]. Experimental schemes include spontaneous emission of atom pairs by collisional de-excitation[9] or four-wave mixing[10–12]. Stimulated emission into twin-modes has been demonstrated in seeded four-wave mixing[2,6], and parametric amplification in optical lattices[7,8] or spinor condensates[13]. Among these schemes, suppression of relative number fluctuations could so far be demonstrated only for multi-mode twin-atoms[12]. A different route to non-classical states is provided by ensembles in multi-well potentials that become number-squeezed during their time evolution[20,21].

Here, we demonstrate how collisional de-excitation of a one-dimensional degenerate Bose gas can be used to efficiently create matter-wave beams of twin-atoms. The restricted geometry of a waveguide potential forces emission of the beams into a single transversal mode, in analogy to an optical parametric amplifier[4]. We prepare the initial population inversion to a radially excited state by shaking the trap, employing an optimal control strategy. Time-of-flight fluorescence imaging is used to directly observe the suppressed relative number fluctuations in the emitted beams.

The starting point of our investigations is a dilute, quantum degenerate gas of neutral rubidium-87 atoms magnetically trapped in a tight waveguide potential with a shallow axial harmonic confinement ($\nu_x = 16.3\,\mathrm{Hz}$) on an atom chip[22]. Our scheme relies on an effective two-level system in the radial vibrational eigenstates of the waveguide. This is accomplished by creating unequal level spacings in the radial yz-plane by radio frequency dressing[23], which introduces anharmonicity and anisotropy. The resulting single-particle first and second excited state energies are $E_{y,z}{}^{(1)} = h\cdot[1.83, 2.58]\,\mathrm{kHz}$ and $E_{y,z}{}^{(2)} = h\cdot[3.82, 5.22]\,\mathrm{kHz}$. As the level spacings increase at higher levels, the ground state $|n_y, n_z; k_x\rangle = |0,0;0\rangle$ ($n_{y,z}$ and k_x denoting the radial quantum numbers and the axial momentum, respectively) and the first excited state along y, $|1,0;0\rangle$ have the lowest energy difference among all possible combinations (Fig. 1a), establishing a closed two-level system.

Using standard techniques we generate a Bose gas of typically 700 atoms at a temperature $T \lesssim 40\,\mathrm{nK} \approx h/k_\mathrm{B}\cdot 830\,\mathrm{Hz}$ (obtained independently from fits to a non-excited degenerate gas[24] and its residual thermal fraction[25]). The thermal occupation of state $|1,0;0\rangle$ is negligible, and the chemical potential quantifying the mean-field interaction is $\mu \sim h\cdot 500\,\mathrm{Hz} \ll E_y{}^{(1)}$. Our Rb sample is therefore a one-dimensional, weakly interacting quasi-Bose–Einstein condensate (quasi-BEC, Lieb–Liniger $\gamma \sim 0.008$; ref. 14), which can be seen as a locally coherent matter wave[26] with a coherence length approximately one order of magnitude below the system size.

Having prepared the gas, we create a population inversion by transferring the quasi-BEC almost entirely to state $|1,0;0\rangle$ (see Fig. 1a). The transition is driven by shaking the trap along the radial y-direction on the scale of the ground state size ($\sim$100 nm). The trajectory (total duration 5 ms, see Fig. 2a) has been optimized by employing an iterative optimal control algorithm (see Supplementary Information). In the experiment, the displacement is achieved by driving a current in an auxiliary chip wire parallel to the main trapping wire.

We monitor the radial momentum distribution of the quasi-BEC by releasing the cloud from the trapping potential at different times t, during and after the excitation pulse. Images are taken after 46 ms of ballistic expansion (Fig. 2b), using a single-atom-sensitive fluorescence imaging system[27]. After the excitation, we observe a small residual beating between the macroscopically occupied $|1,0;0\rangle$ state and a remaining non-excited population in $|0,0;0\rangle$. From a fit to the beating pattern (Fig. 2c) we estimate an efficiency of the coherent transfer of $\eta_\mathrm{e} \approx 97\%$ and deduce the energy difference $\epsilon = h\cdot 1.78\,\mathrm{kHz}$ between $|0,0;0\rangle$ and $|1,0;0\rangle$ (see Methods). The slight deviation between $E_y{}^{(1)}$ and ϵ is explained by particle interactions. A calculation based on the one-dimensional Gross–Pitaevskii equation (GPE) (Fig. 2d) shows excellent agreement with the observed dynamics.

The population inversion to $|1,0;0\rangle$ represents a highly non-equilibrium state of the system, analogous to a laser gain medium

[1]Vienna Center for Quantum Science and Technology, Atominstitut, TU Wien, 1020 Vienna, Austria, [2]Institut für Physik, Karl-Franzens-Universität Graz, 8010 Graz, Austria, [3]Wolfgang Pauli Institut, 1090 Vienna, Austria. †Present addresses: Theoretische Chemie, Physikalisch-Chemisches Institut. Universität Heidelberg, Germany (J.G.); Laboratoire de Physique des Lasers, Institut Galilée, Université Paris 13, Villetaneuse, France (A.P.). *e-mail: schmiedmayer@atomchip.org.

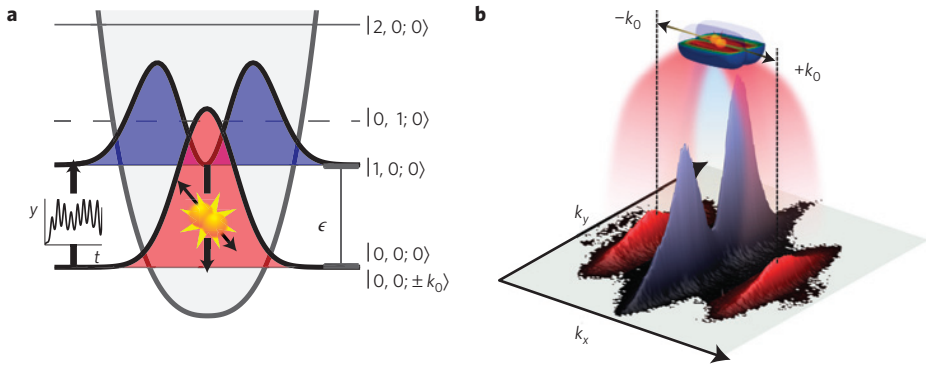

Figure 1 | Schematic of the excitation and emission process. a, The quasi-BEC is transferred from the ground state $|0,0;0\rangle$ into $|1,0;0\rangle$, the first excited state of the trapping potential along the radial y-direction. This is accomplished by means of a fast non-adiabatic movement of the potential minimum along an optimized trajectory (inset). The excited state decays by emission of twin-atoms into the radial ground state modes $|0,0;\pm k_0\rangle$. **b**, After excitation and pair emission, the cloud is released from the trapping potential and imaged after expansion. The central part of the system clearly shows the spatial structure of the radially excited state (blue). Two clouds containing the twin-atoms (red) are emitted.

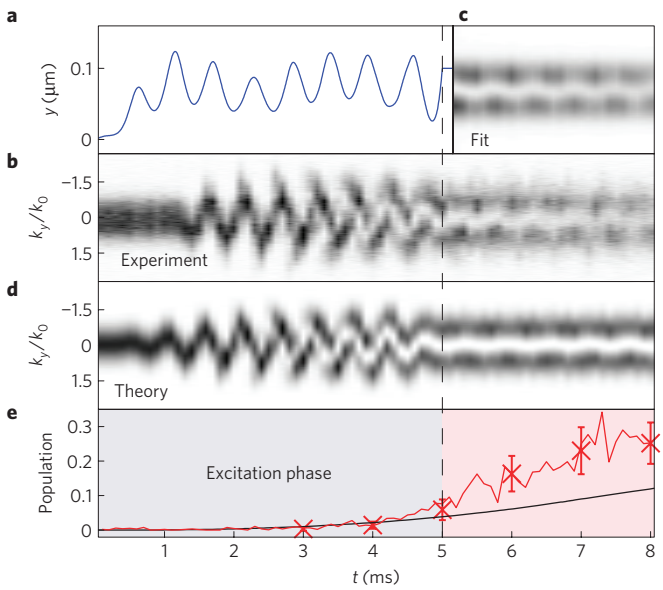

Figure 2 | Dynamics of the excitation and emission process: comparison between theory and experiment. a, Optimized control trajectory for the trap movement along y. **b**, Measured momentum distribution. Fluorescence images integrated along k_x over a region encompassing the central cloud. Average over five experimental runs. **c**, Fit of the time-dependent momentum distribution, scaled to the experimental total density at each time step. **d**, Calculated momentum distribution, using a one-dimensional GPE model. As the model does not take into account the pair emission process, agreement with the experiment is expected approximately up to the end of the excitation pulse. **e**, Red line: Population of the emitted clouds obtained from the same data set as **b**. Red crosses: population of the emitted clouds obtained from a separate measurement with 100 experimental runs each (error bars represent the ensemble standard deviation). Black line: theoretical estimation for spontaneous processes only.

after a pump pulse. For the ensuing relaxation, the only allowed channel is a two-particle collisional process, emitting atom pairs with opposite momenta. In contrast to experiments with free-space collisions[10,12] or two-dimensional gases[9], the constricted geometry and non-degenerate level scheme of our source restricts the outgoing matter waves to the radial ground state of the waveguide, yielding twin-atom beams in a single transversal mode. Within a binary collision, two atoms are scattered from $|1,0;0\rangle\,|1,0;0\rangle$ to $|0,0;+k_0\rangle\,|0,0;-k_0\rangle$, where energy conservation requires the final momenta to be centred around $\pm k_0 = \pm\sqrt{2\,m\epsilon}/\hbar$. The emission process can be understood as a matter-wave analogue of a degenerate optical parametric amplifier, where the initially empty twin-modes are seeded by vacuum fluctuations[4] and have an exponentially growing population if phase matching conditions are fulfilled. Owing to the finite size, the axial multi-mode character of the quasi-BEC source[14], and the depletion of the initial state, a comprehensive understanding of the process is challenging. The emission dynamics, as well as the ensuing longitudinal coherence properties of the beams (which should resemble those of the source), will be the subject of future experimental and theoretical studies. A comparison of the observed rates to a simple calculation using Fermi's golden rule (see Supplementary Information) is shown in Fig. 2e and demonstrates the insufficiency of a purely spontaneous model (in contrast to the findings of ref. 9 for a transversal multi-mode system).

Once the trap potential is switched off and the atoms propagate freely (Fig. 1b), the twin-beam modes can be detected essentially background-free in fluorescence images (Fig. 3a,b) as they separate from the source. In Fig. 3c, the radial momentum distribution of the twin-beams is compared to an independent measurement of the initial $|0,0;0\rangle$ cloud. The small deviation is attributed to a slight overlap of the central cloud with the integration regions of the emitted clouds (red boxes in Fig. 3b) and interactions with the mean field of the quasi-BEC in the $|1,0;0\rangle$ state. Furthermore, an excited cloud at $t = 6$ ms is shown. From the axial position of the side peaks (Fig. 3d) we can deduce an emitted atom momentum of $k_0 = 2\pi \cdot 0.883(3)\ \mu\text{m}^{-1}$, equivalent to $\epsilon = h \cdot 1.78(1)$ kHz, in perfect agreement with the value determined from the beating fit (Fig. 2c). The width of the emitted clouds (Fig. 3d) is increased by a factor of $\approx$1.4 with respect to the source cloud. At momenta corresponding to $\epsilon' \approx h \cdot 3.9$ kHz, further, very weakly populated atom clouds ($\lesssim$1 atom per image) are observed on an averaged picture (Fig. 3b). They imply a transient population of $|2,0;0\rangle$ during the control sequence that directly decays into the radial ground state. In the following analysis, they are merged with the atoms originating from $|1,0;0\rangle$.

The non-classical correlation in the emitted twin-atom beams is revealed by a sub-binomial distribution of the number imbalance $n = N_1 - N_2$ between atoms detected at $\pm k_0$. The variance of n can be expressed as $\sigma_n{}^2 = \xi^2 \bar{N}$, where $\bar{N}$ denotes the mean total atom number in the emitted clouds. The noise reduction factor ξ^2 quantifies the suppression of $\sigma_n{}^2$ with respect to a binomial distribution and, thus, the amount of correlation between the populations N_1 and N_2.

In the fluorescence images, we count photons in regions encompassing the emitted clouds that were released at $t = 7$ ms.

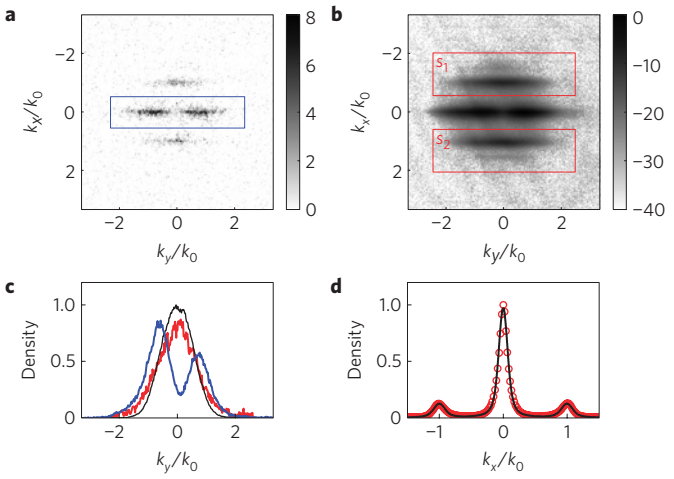

Figure 3 | Atom cloud image analysis. a, Typical experimental image of ~700 atoms released from the trap 7 ms after starting the excitation sequence. The cloud is allowed to expand for 46 ms, making the initial momentum distribution accessible. The quasi-BEC in the excited state $|1,0;0\rangle$ is clearly distinct from the emitted clouds at momenta $\pm\hbar k_0$. Units are photons per pixel. The blue box indicates the integration range for the data shown in Fig. 2b. **b**, Average over ≈1,500 images similar to **a**. The colour scale is logarithmic (dB referenced to peak density). The regions used for correlation analysis are indicated as red boxes. **c**, Normalized, radial momentum distributions of the central (blue) and emitted (red) clouds. Average of 50 images of clouds released at $t = 6$ ms. As comparison, the distribution of a non-excited cloud is shown (black, average over 100 images). **d**, Normalized profile of **b** along k_x (red dots) and three-peak fit (black line) based on stochastic simulations[24].

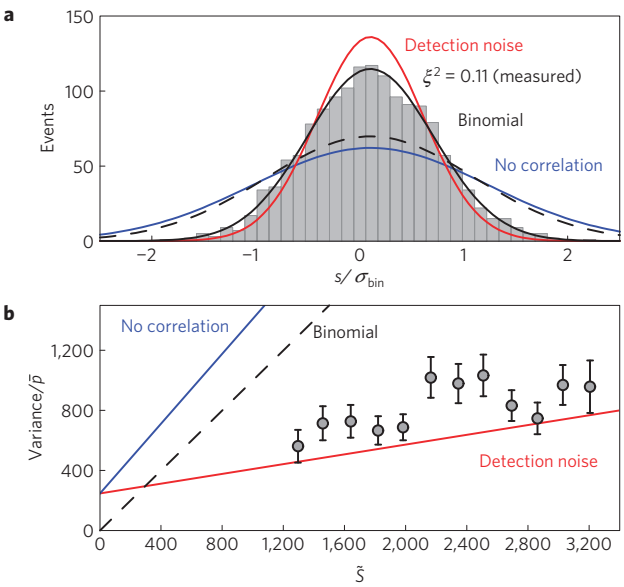

Figure 4 | Correlation analysis. a, Histogram of observed signal imbalances s between the emitted clouds, in units of the binomial standard deviation $\sigma_{bin} = (\bar{p}\bar{S})^{1/2}$. The curves indicate normal distributions corresponding to the experimental result of $\xi^2 = 0.11(2)$ (black, solid); the limits of perfect correlation, where only detection noise remains (red, solid); of uncorrelated signals, defining the reference point for ξ^2 (blue, solid); and a binomial distribution for $\bar{p}\bar{S}$ trials (black, dashed). **b**, Observed signal imbalance variances for data bins corresponding to different total signal in the emitted clouds $\bar{S}$. Error bars are the standard error. The lines correspond to those in **a**. The corrected variances are given by the vertical distances between the data points and the detection noise.

For given atom numbers $N_{1,2}$, the expectation values for the photon numbers are $S_{1,2} = \bar{p}N_{1,2} + \bar{b}/2$, where $\bar{p} = 12.3(9)$ denotes the average number of photons per atom and $\bar{b}/2$ accounts for background events. Our main observable is the variance ${\sigma_s}^2$ of the signal imbalance $s = S_1 - S_2$. Its expectation value for a binomial distribution of atoms and noise-free detection is given by ${\sigma_{bin}}^2 = \bar{p}\bar{S}$, where $\bar{S} = \bar{S_1} + \bar{S_2} - \bar{b}$. From the experimental data as shown in Fig. 4a we obtain an uncorrected reduction factor ${\sigma_s}^2/{\sigma_{bin}}^2 = 0.37(3)$. However, a significant contribution to ${\sigma_s}^2$ originates not from the atom number fluctuations, but from the detection process itself. For fluorescence imaging as employed in our experiment, this contribution can be directly calculated from the photon shot noise and detection background (see Methods). It is accounted for by subtracting a correction ${\sigma_d}^2$ from ${\sigma_s}^2$. From the corrected variances, we infer a reduction factor of $\xi^2 = ({\sigma_s}^2 - {\sigma_d}^2)/{\sigma_{bin}}^2 = 0.11(2)$, which is the main result of this paper. It is equivalent to an intensity squeezing in the sense of ref. 4. In strong contrast to the suppressed relative fluctuations, applying an analogous calculation on the variance ${\sigma_S}^2$ of the summed signal in the emitted clouds $S = S_1 + S_2$ (binned into groups with similar total atom number) yields super-Poissonian fluctuations $({\sigma_s}^2 - {\sigma_d}^2)/\bar{p}\bar{S} \sim 7$, highlighting the presence of bosonic amplification.

To study the correlation data in more detail, we bin the experimental shots according to the emitted atom signal S and calculate the variances ${\sigma_s}^2$ and mean signals $\bar{S}$ for each bin (consisting of typically 100 runs) separately, as shown in Fig. 4b. The differences between the data points and the detection noise ${\sigma_d}^2$ represent the corrected variances, as introduced above. They seem to be independent of $\bar{S}$, which is supported by χ^2-test results on various plausible models. As any uncorrelated emissions should scale with $\bar{S}$, this suggests that the non-zero value of ξ^2 can be explained by a slight additional background signal, for example as a result of the residual overlap of the excited quasi-BEC and the emitted clouds.

The availability of single-mode twin-atom beams adds an essential building block for quantum matter-wave optics. As our scheme does not rely on the internal structure of the atoms, it can be applied to any sufficiently controllable system of interacting bosons. Possible applications include interferometry with dual-Fock states[15], Hong–Ou–Mandel-type experiments[17] or continuous-variable entanglement[5,19]. Inclusion of internal (for example, hyperfine states with appropriate scattering properties) or few-mode external (for example, two-mode double well states) degrees of freedom seems a viable strategy to generate non-local entangled states of massive particles for Bell-type measurements[16,18,19,28,29].

Methods

Trap potential preparation. We trap our atoms in an adiabatic dressed state potential[23], created on an atom chip[22]. The radial potential can be approximated by quartic polynomials, where the x^4-term typically contributes ≈5% at relevant length scales (see Supplementary Information for details).

Radial excitation. We use optimal control of the one-dimensional (along y) GPE (ref. 30) to derive the shape of the excitation pulse. The anharmonicity of the radial potential enables transfer to the population-inverted state, as opposed to a harmonic potential in which only coherent states can be excited by displacement. To obtain the excitation efficiency $\eta_e = 0.97$ and $\epsilon = h \cdot 1.78$ kHz from the beating between $|0,0;0\rangle$ and $|1,0;0\rangle$ we fit a superposition of the $\psi_1(k_y) = \langle k_y|1,0;0\rangle$ and $\psi_0(k_y) = \langle k_y|0,0;0\rangle$ wavefunctions with a time-dependent relative phase $\epsilon/\hbar \cdot t$ to the momentum density of the central cloud (Fig. 2b,c). Starting from about $t \approx 5$ ms, the contrast of the beating pattern starts to fade (Fig. 2b), which is attributed to dephasing collisions between emitted atoms and the main cloud. This is taken into account by (incoherently) adding a contribution $|\psi_0(k_y)|^2$ to the density fit, with a linearly growing population reaching ≈28% at the latest time measured. Note, however, that this does not affect the efficiency of the excitation itself.

Imaging characterization. The fluorescence imaging system[27] is calibrated by comparing a large number of fluorescence and calibrated absorption images of identically prepared clouds. As absorption images yield an absolute atom number, we can determine the number of photons per atom to $\tilde{p} = 12.3(9)$. This value is compatible with independent measurements of the physical properties of three-dimensional clouds[25]. The detection noise ${\sigma_d}^2$, which is used to correct the observed number fluctuations, can be split into a constant and a signal-dependent part (see red line in Fig. 4b). The constant part is given by background events and readout noise ${\sigma_b}^2 \approx 2\tilde{b}$, which can be obtained from empty regions in the images next to the atoms. The signal-dependent contribution is defined by the variance of the photon number per atom ${\sigma_p}^2$. Photon shot noise and amplification noise of the Electron Multiplying Charge Coupled Device (EMCCD) camera used yields ${\sigma_p}^2 = 2\tilde{p}$ (see Supplementary Information and ref. 27). In total, we arrive at ${\sigma_d}^2 = {\sigma_p}^2\tilde{N} + {\sigma_b}^2 = 2\tilde{S} + {\sigma_b}^2$.

Received 8 February 2011; accepted 31 March 2011; published online 1 May 2011

References

1. Cronin, A., Schmiedmayer, J. & Pritchard, D. Optics and interferometry with atoms and molecules. *Rev. Mod. Phys.* **81,** 1051–1129 (2009).
2. Deng, L. *et al.* Four wave mixing with matter waves. *Nature* **398,** 218–220 (1999).
3. Orzel, C., Tuchman, A. K., Fenselau, M. L., Yasuda, M. & Kasevich, M. A. Squeezed states in a Bose–Einstein condensate. *Science* **291,** 2386–2389 (2001).
4. Heidmann, A. *et al.* Observation of quantum noise reduction on twin laser beams. *Phys. Rev. Lett.* **59,** 2555–2557 (1987).
5. Reid, M. D. *et al.* Colloquium: The Einstein–Podolsky–Rosen paradox: From concepts to applications. *Rev. Mod. Phys.* **81,** 1727–1751 (2009).
6. Vogels, J., Xu, K. & Ketterle, W. Generation of macroscopic pair-correlated atomic beams by four-wave mixing in Bose–Einstein condensates. *Phys. Rev. Lett.* **89,** 020401 (2002).
7. Gemelke, N., Sarajlic, E., Bidel, Y., Hong, S. & Chu, S. Parametric amplification of matter waves in periodically translated optical lattices. *Phys. Rev. Lett.* **95,** 170404 (2005).
8. Campbell, G. K. *et al.* Parametric amplification of scattered atom pairs. *Phys. Rev. Lett.* **96,** 020406 (2006).
9. Spielman, I. B. *et al.* Collisional deexcitation in a quasi-two-dimensional degenerate bosonic gas. *Phys. Rev. A* **73,** 020702 (2006).
10. Perrin, A. *et al.* Observation of atom pairs in spontaneous four-wave mixing of two colliding Bose–Einstein condensates. *Phys. Rev. Lett.* **99,** 150405 (2007).
11. Dall, R. G. *et al.* Paired-atom laser beams created via four-wave mixing. *Phys. Rev. A* **79,** 011601 (2009).
12. Jaskula, J-C. *et al.* Sub-Poissonian number differences in four-wave mixing of matter waves. *Phys. Rev. Lett.* **105,** 190402 (2010).
13. Klempt, C. *et al.* Parametric amplification of vacuum fluctuations in a spinor condensate. *Phys. Rev. Lett.* **104,** 195303 (2010).
14. Petrov, D. S., Shlyapnikov, G. V. & Walraven, J. T. M. Regimes of quantum degeneracy in trapped 1d gases. *Phys. Rev. Lett.* **85,** 3745–3749 (2000).
15. Dunningham, J., Burnett, K. & Barnett, S. Interferometry below the standard quantum limit with Bose–Einstein condensates. *Phys. Rev. Lett.* **89,** 150401 (2002).
16. Horne, M. A., Shimony, A. & Zeilinger, A. Two-particle interferometry. *Phys. Rev. Lett.* **62,** 2209–2212 (1989).
17. Hong, C. K., Ou, Z. Y. & Mandel, L. Measurement of subpicosecond time intervals between two photons by interference. *Phys. Rev. Lett.* **59,** 2044–2046 (1987).
18. Rarity, J. & Tapster, P. Experimental violation of Bell's inequality based on phase and momentum. *Phys. Rev. Lett.* **64,** 2495–2498 (1990).
19. Gneiting, C. & Hornberger, K. Bell test for the free motion of material particles. *Phys. Rev. Lett.* **101,** 260503 (2008).
20. Estève, J., Gross, C., Weller, A., Giovanazzi, S. & Oberthaler, M. K. Squeezing and entanglement in a Bose–Einstein condensate. *Nature* **455,** 1216–1219 (2008).
21. Maussang, K. *et al.* Enhanced and reduced atom number fluctuations in a BEC splitter. *Phys. Rev. Lett.* **105,** 080403 (2010).
22. Folman, R., Krüger, P., Schmiedmayer, J., Denschlag, J. & Henkel, C. Microscopic atom optics: From wires to an atom chip. *Adv. At. Mol. Opt. Phys.* **48,** 263–356 (2002).
23. Schumm, T. *et al.* Matter wave interferometry in a double well on an atom chip. *Nature Phys.* **1,** 57–62 (2005).
24. Stimming, H-P., Mauser, N., Schmiedmayer, J. & Mazets, I. Fluctuations and stochastic processes in one-dimensional many-body quantum systems. *Phys. Rev. Lett.* **105,** 015301 (2010).
25. Perrin, A. *et al.* Hanbury Brown and Twiss correlations across the Bose–Einstein condensation threshold. Preprint at http://arXiv.org/1012.5260 (2010).
26. Hofferberth, S., Lesanovsky, I., Fischer, B., Schumm, T. & Schmiedmayer, J. Non-equilibrium coherence dynamics in one-dimensional Bose gases. *Nature* **449,** 324–327 (2007).
27. Bücker, R. *et al.* Single-particle-sensitive imaging of freely propagating ultracold atoms. *New J. Phys.* **11,** 103039 (2009).
28. Pu, H. & Meystre, P. Creating macroscopic atomic Einstein–Podolsky–Rosen states from Bose–Einstein condensates. *Phys. Rev. Lett.* **85,** 3987–3990 (2000).
29. Duan, L-M., Sørensen, A., Cirac, J. I. & Zoller, P. Squeezing and entanglement of atomic beams. *Phys. Rev. Lett.* **85,** 3991–3994 (2000).
30. Hohenester, U., Rekdal, P. K., Borzì, A. & Schmiedmayer, J. Optimal quantum control of Bose–Einstein condensates in magnetic microtraps. *Phys. Rev. A* **75,** 023602 (2007).

Acknowledgements

We acknowledge support from the FWF projects P21080-N16 and I607, the EU projects AQUTE, QuDeGPM and Marie Curie (FP7 GA no. 236702), the FWF doctoral programme CoQuS (W 1210), the FunMat and NAWI GASS research alliances, the City of Vienna and Siemens Austria. We wish to thank E. Altman, A. Gottlieb, B. Hessmo, K. Kheruntsyan, I. Mazets, M. Oberthaler, H. Ritsch and G. von Winckel for stimulating discussions.

Author contributions

R.B., S.M. and T. Berrada collected the data presented in this letter. J.G. and U.H. provided the OCT calculations for the excitation sequence. All authors contributed to analysis and interpretation of the data and helped in editing the manuscript.

Additional information

The authors declare no competing financial interests. Supplementary information accompanies this paper on www.nature.com/naturephysics. Reprints and permissions information is available online at http://www.nature.com/reprints. Correspondence and requests for materials should be addressed to J.S.

nature physics

SUPPLEMENTARY INFORMATION

DOI: 10.1038/NPHYS1992

Twin-atom beams

R. Bücker *et al.*

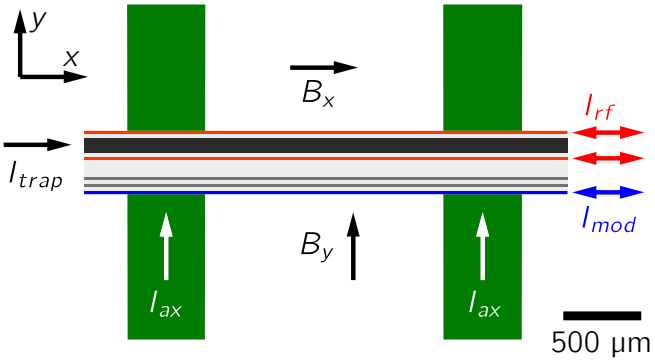

FIG. 1. Schematic of the atom chip layout. The waveguide potential is formed by the current I_{trap} through the main trapping wire (black) and a static magnetic field B_y. On a separate chip layer, currents I_{ax} in broad wires (green) provide axial confinement. An external field B_x completes the Ioffe-Pritchard configuration. The radio frequency dressing currents I_{rf} are applied to wires (red) in parallel to the trapping wire. Finally, the modulation of the trap position is accomplished by a current I_{mod} in an auxiliary wire (blue).

Preparation of the trapping potential

Both the optimized excitation scheme needed for transferring the quasi-BEC into $|1,0;0\rangle$ (see next section), and restricting the emission to a single transverse mode $|0,0;\pm k_0\rangle$ require a sufficiently anharmonic trapping potential along y with increasing level spacings. Hence, the initially radially symmetric Ioffe-Pritchard field configuration created by our chip wire configuration (see [1] and figure 1) is being modified by radio frequency dressing [2, 3]. Typically used for creating double well potentials, this technique also allows for the introduction of anharmonicity and anisotropy to a single trap when the dressing strength is kept slightly below the point where actual splitting of the potential occurs. We apply an ac current of $I_{rf} = 23\,\mathrm{mA}$ peak-to-peak amplitude at a detuning of $\delta = -54\,\mathrm{kHz}$ with respect to the atomic Larmor frequency near the trap minimum ($\nu_0 = 824\,\mathrm{kHz}$) to two wires running on each side of the main trapping wire at a distance of 55 µm.

The resulting potential can be calculated numerically by means of a Floquet analysis [4]. In the two radial directions it can be approximated by quartic polynomials of the form $E = p_4 r^4 + p_2 r^2$: In the y-direction, along which the excitation is performed the coefficients are $p_4 = h \cdot 13.1\,\mathrm{Hz/r_0^4}$ and $p_2 = h \cdot 343\,\mathrm{Hz/r_0^2}$. In the z-direction perpendicular to the excitation motion the coefficients are $p_4 = h \cdot 10.4\,\mathrm{Hz/r_0^4}$ and $p_2 = h \cdot 793\,\mathrm{Hz/r_0^2}$. Here, $r_0 = 172\,\mathrm{nm}$ is the mean radial ground state radius as calculated by the Gross-Pitaevskii equation.

Along the axial x-axis, the trap frequency given in the text is determined by observation of a deliberately excited sloshing mode of the quasi-BEC.

Optimized excitation of the condensate

To transfer the cloud into the radially excited state $|1,0;0\rangle$ we displace the radial trap minimum along an optimized trajectory.

This movement is achieved by applying a current of typically less than 10 mA to a wire parallel to the trapping wire at 140 µm distance (see figure 1). The resulting magnetic field is mostly oriented along the z-direction at the cloud position, moving the potential predominantly along y [5]. The calculated offset is 26 nm/mA along y and 9 nm/mA along z, where the contribution along z does not significantly distort the excitation process (see below).

The most efficient way of moving the trap for excited state preparation is obtained from numerical calculations which employ *optimal control* [6] of the Gross-Pitaevskii equation. Optimal control theory is a powerful tool which allows to minimize a given cost functional with the constraint that the system is governed by the corresponding equations of motion. In our case, we iteratively solved an optimal control system determined from a Lagrangian framework [6, 7]. For *desired state trapping* one maximizes the overlap of the wave function at the final time with a given desired state. This has been used before in theoretical works about transferring or splitting a BEC by continuously transforming a trap potential from an initial to a final shape, *without* exciting the BEC [8, 9]. In the present work, we employ the same techniques, but choose the first excited state of the Gross-Pitaevskii equation at the final trap position as desired state.

For such excited state preparation, it is crucial to use an anharmonic trap, as for a weakly interacting system in a harmonic trap, displacements generate displaced ground states, i.e., coherent states. The present optimal control calculations have been performed in 1D (along y) for simplicity, using an effective 1D interaction parameter [10]. This works well, since the dynamics in the axial x-direction is orders of magnitudes slower than in the radial ones. Moreover, the potential is sufficiently anisotropic

DOI: 10.1038/NPHYS1992

in the radial plane, such that the z direction is not significantly affected by the movement, even though it is not strictly performed along y (see above). We performed 2D simulations of the Gross-Pitaevskii equation and found only small deviations as compared to the 1D case.

To estimate the excitation efficiency from experimental data we fit a model of the time-dependent momentum density along y in the main cloud (i.e. not including the emitted atoms) after the excitation pulse (see figure 2b,c in the main text), according to

$$n(k_y,t) = (1-\eta_d(t))|\sqrt{1-\eta_e}\psi_0(k_y) + \sqrt{\eta_e}e^{i\epsilon/\hbar\cdot t}\psi_1(k_y)|^2 + \eta_d(t)|\psi_0(k_y)|^2,$$

where the total density of the experimental data is normalized for each time step. The first line corresponds to the coherent two-level dynamics between the radially excited state $\psi_1(k_y) = \langle k_y|1,0;0\rangle$ and the ground state $\psi_0(k_y) = \langle k_y|0,0;0\rangle$ at a beating frequency given by the single-particle energy difference $\epsilon \approx E_y^{(1)}$. The efficiency of excitation is denoted as η_e. In the second line, an incoherent admixture of the ground state is added with a time-dependent population $\eta_d(t)$, which corresponds to dephased atoms having undergone emission into the $|0,0;\pm k_0\rangle$ modes and subsequent collisions with the excited main cloud. The momentum-space wave functions ψ_1 and ψ_0 correspond to eigenstates of the one-dimensional Gross-Pitaevskii equation at a typical atom number. From the fit we deduce an efficiency of the coherent excitation of $\eta_e = 0.97$ and a dephased fraction linearly rising from $\eta_d(5.2\,\mathrm{ms}) = 0.08$ to $\eta_d(8\,\mathrm{ms}) = 0.28$. For the energy difference we obtain $\epsilon = h \cdot 1.78\,\mathrm{kHz}$.

Emission dynamics model

We compare the fraction of emitted high-momentum atoms to a simple model, taking into account spontaneous emission only, and assuming an atom number corresponding to the average of the shown dataset ($\bar{N}_{tot} \approx 700$). To obtain the theory curve, we solve rate equations between the states $|0,0;0\rangle$, $|1,0;0\rangle$ and $|0,0;\pm k_0\rangle$. The excitation rate from $|0,0;0\rangle$ to $|1,0;0\rangle$ cannot be directly obtained from GPE calculations, as both the populations of the radial states as well as their wave functions are time-dependent. It is thus approximated by a constant rate during the excitation pulse. On the other hand, to treat the emission from $|1,0;0\rangle$ to $|0,0;\pm k_0\rangle$, we assume an axial density distribution according to [11] and employ Fermi's golden rule for indistinguishable bosons to obtain a weakly atom-number-dependent two-body decay constant of the order of $\Gamma_{em}[N_{exc}] \sim 0.05\mathrm{s}^{-1}$. This allows to estimate the emission rate as $\dot{N} = 2\Gamma_{em}[N_{exc}(t)]N_{exc}(t)^2$, where N_{exc} denotes the number of atoms in $|1,0;0\rangle$, calculated as described before. While during the initial phase, where $N_{exc}, N \ll N_{tot}$ the model works well, it fails at later times where $N_{exc}, N \lesssim N_{tot}$, indicating that stimulated processes have to be taken into account, analogous to parametric amplification in quantum optics.

Fluorescence detection and noise corrections

To detect the atoms after release from the trapping potentials we employ a fluorescence detector introduced in [12]. The expanding cloud falls through a thin horizontal light sheet (vertical waist radius $w_0 = 20\,\mu\mathrm{m}$) after 46 ms of expansion time. Light scattered by the atoms is collected by an objective outside the vacuum vessel and imaged on an EMCCD camera. The extraordinarily low background of the system enables single-atom sensitivity while maintaining the dynamic range needed for imaging of dense Bose-Einstein condensates. For the excitation power employed (which is of the order of the atomic saturation intensity at the centre of the light sheet), $\bar{p} = 12.3 \pm 0.9$ photons per atom are detected on average. This number is deduced from cross-calibration by comparison of a sufficient number of calibrated absorption imaging and fluorescence shots of clouds prepared under identical conditions. It is compatible with independent estimates obtained from physical properties of clouds released from a nearly isotropic trap [13]. Slight dependencies of $\bar{p}$ on the spatial position within the image due to CCD etaloning and inhomogeneity of the illumination can be corrected by using a reference image.

For exact analysis of the pair correlation as described below, also the variance of the distribution of photons per atom σ_p^2 has to be estimated. The first contribution to this variance is the photon shot noise $\sigma_{SN}^2 = \bar{p}$. Furthermore, the excess noise due to the stochastic amplification in the EMCCD detector has to be taken into account and increases the detection noise by a factor of two [14]: $\sigma_{amp}^2 = 2\bar{p}$, in accordance to independent characterization measurements using Poissonian light sources and the value for the detection background (see below). Finally, a further broadening of the distribution of p is caused by the diffusion of atoms within the light sheet [12]. However, this contribution is hard to obtain from experimental results (as we cannot prepare single atoms deterministically as e.g. in [15]) and can only be estimated from simulations. To avoid overestimation of detection noise, which would spuriously reduce ξ^2, we assume $\sigma_p^2 = \sigma_{amp}^2$ and set $\sigma_p^2/\bar{p} = 2$ in our analysis.

Apart from the distribution of p, another detection contribution to σ_s^2 originates from the residual background signal b. We extract $\bar{b}$ and σ_b^2 from regions directly adjacent to the main analysis regions, which contain the emitted clouds and scale the obtained values accordingly. We obtain $\sigma_b^2/\bar{b} = 2.14$, which can be understood as combined effect of shot and amplification noise and residual readout noise. Again, to avoid over-correction, we

make sure that the background treatment does not lead to spurious reduction of ξ^2 when the analysis regions are enlarged artificially.

Correlation analysis

As a first step to determine the amount of population correlation between the emitted clouds, we count the photon numbers S_1, S_2 (indicating atom numbers N_1, N_2) within regions encompassing them (see figure 3b in the main article). Choosing the integration range along the axial x-direction is a sensitive task, as a too small region will not capture all emitted atoms, deteriorating the result. On the other hand, one has to take into consideration residual overlap of the emitted clouds with the quasi-BEC. As expected, we find that setting the limit to the position of the density minimum between main and emitted clouds minimizes the obtained value of ξ^2. Still the residual overlap appears to be one of the limiting factors to the measurable correlation. The outer limits are chosen in a way that the weak clouds emitted from $|2,0;0\rangle$ (on average less then one atom per image) are still contained within the analysis regions. Those overlap significantly with the main emitted clouds, thus limiting the ability to assess the correlations between them separately.

To calculate ξ^2 from the accessible quantities σ_s^2 and $\tilde{S}$, as defined in the text, we have to estimate the total contribution of detection noise σ_d^2 from the quantities σ_b^2 and σ_p^2 as defined in the previous section. We can decompose σ_s^2 into a population fluctuation term and a detection term using the law of total variance:

$$\begin{aligned}\mathrm{Var}(s) =&\mathrm{Var}(\mathrm{E}(s|n)) + \mathrm{E}(\mathrm{Var}(s|n))\\ =&\mathrm{Var}(\mathrm{E}(p)n) + \mathrm{E}(\mathrm{Var}(p)N + \mathrm{Var}(b)),\end{aligned}$$

where b and p are the background signal and the number of photons per atom as discussed above, $s = S_1 - S_2$, $n = N_1 - N_2$, $N = N_1 + N_2$. $\mathrm{E}(X)$ and $\mathrm{Var}(X)$ denote expectation value and variance of the random variable X. For our analysis, assuming $\mathrm{Var}(X) = \sigma_X^2$ and $\mathrm{E}(X) = \overline{X}$, this reads

$$\begin{aligned}\sigma_s^2 =&\bar{p}^2\xi^2\bar{N} + \sigma_p^2\bar{N} + \sigma_b^2\\ =&\bar{p}\xi^2\tilde{S} + v\tilde{S} + \sigma_b^2\\ =&\xi^2\sigma_{bin}^2 + \sigma_d^2,\end{aligned}$$

and thus $\sigma_d^2 = v\tilde{S} + \sigma_b^2$. Solving for ξ^2 leads to the formula used for the analysis.

To estimate the uncertainty of ξ^2 we propagate the standard error of the shot-to-shot mean of b, σ_b^2, S and p, the latter obtained from an independent measurement as described earlier. The error of $\sigma_s^2 = (k-1)^{-1}\sum_{m=1}^{k}(s_m - \bar{s})^2$, where k denotes the number of experimental runs, is calculated as $\sigma_s^2 \cdot (2/(k-1))^{1/2}$.

[1] Trinker, M. *et al.* Multilayer atom chips for versatile atom micromanipulation. *Appl. Phys. Lett.* **92**, 254102 (2008).

[2] Lesanovsky, I. *et al.* Adiabatic radio-frequency potentials for the coherent manipulation of matter waves. *Phys. Rev. A* **73**, 33619 (2006).

[3] Schumm, T. *et al.* Matter wave interferometry in a double well on an atom chip. *Nature Phys.* **1**, 57–62 (2005).

[4] Shirley, J. H. Solution of the Schrödinger Equation with a Hamiltonian Periodic in Time. *Phys. Rev.* **138**, B979–B987 (1965).

[5] Folman, R., Krüger, P., Schmiedmayer, J., Denschlag, J. & Henkel, C. Microscopic atom optics: from wires to an atom chip. *Adv. At. Mol. Opt. Phys.* **48**, 263–356 (2002).

[6] Peirce, A. P., Dahleh, M. A. & Rabitz, H. Optimal control of quantum-mechanical systems: Existence, numerical application, and applications. *Phys. Rev. A* **37**, 4950 (1988).

[7] Borzì, A., Stadler, G. & Hohenester, U. Optimal quantum control in nanostructures: Theory and application to generic three-level system. *Phys. Rev. A* **66**, 053811 (2002).

[8] Hohenester, U., Rekdal, P. K., Borzì, A. & Schmiedmayer, J. Optimal quantum control of Bose-Einstein condensates in magnetic microtraps. *Phys. Rev. A* **75**, 023602 (2007).

[9] von Winckel, G. & Borzì, A. Computational techniques for a quantum control problem with H^1-cost. *Inverse Problems* **24**, 034007 (2008).

[10] Grond, J., von Winckel, G., Schmiedmayer, J. & Hohenester, U. Optimal control of number squeezing in trapped Bose-Einstein condensates. *Phys. Rev. A* **80**, 053625 (2009).

[11] Gerbier, F. Quasi-1D Bose-Einstein condensates in the dimensional crossover regime. *Europhys. Lett.* **66**, 771 (2004).

[12] Bücker, R. *et al.* Single-particle-sensitive imaging of freely propagating ultracold atoms. *New J. Phys.* **11**, 103039 (2009).

[13] Perrin, A. *et al.* Hanbury Brown and Twiss correlations across the Bose-Einstein condensation threshold. *arXiv.org* 1012.5260 (2010).

[14] Basden, A. G., Haniff, C. A. & Mackay, C. D. Photon counting strategies with low-light-level CCDs. *MNRAS* **345**, 985–991 (2003).

[15] Fuhrmanek, A. *et al.* Imaging a single atom in a time-of-flight experiment. *New J. Phys.* **12**, 053028 (2010).